PERGAMON

International Journal of Heat and Mass Transfer 44 (2001) 3397–3412

International Journal of HEAT and MASS TRANSFER

www.elsevier.com/locate/ijhmt

# Fully developed laminar flow in trapezoidal grooves with shear stress at the liquid–vapor interface

Scott K. Thomas [a,*], Richard C. Lykins [a,1], Kirk L. Yerkes [b]

[a] *Department of Mechanical and Materials Engineering, Wright State University, 3640 Colonel Glenn Hwy, Dayton, OH 45435-0001, USA*

[b] *Air Force Research Laboratory (PRPG), Wright–Patterson AFB, OH 45433-7251, USA*

Received 3 August 2000; received in revised form 6 December 2000

**Abstract**

This paper discusses the behavior of liquid flowing in a groove with a trapezoidal cross-section. For fully developed laminar flow, the conservation of mass and momentum equations reduce to the classic Poisson equation in terms of the liquid velocity. A finite difference solution was employed to determine the mean velocity, volumetric flow rate, and Poiseuille number ($Po = fRe$) as functions of the groove aspect ratio, groove-half angle, meniscus contact angle and imposed shear stress at the liquid–vapor interface. Comparisons with existing solutions for fully developed flow in rectangular ducts and rectangular and triangular grooves are provided. The volumetric flow rate in a groove in which the fill amount varies is discussed. A semi-analytical solution and a two-point numerical solution for the mean velocity in a groove are presented and used to determine the capillary limit for a revolving helically grooved heat pipe. The effects of interfacial shear stress and groove fill ratio on heat pipe performance are investigated. 

## 1. Introduction

Internally grooved ducts are used in process equipment to improve heat transfer during condensation and evaporation. In some cases, such as a refrigeration cycle evaporator or condenser with internal grooves, the vapor flow is cocurrent with respect to the liquid flow. In axially grooved heat pipes, the vapor flow is countercurrent to the liquid flow. The interfacial shear stress due to the cocurrent or countercurrent vapor flow contributes to the liquid pressure drop, which can significantly affect the heat transfer capacity of the grooved surface. The objective of the present research was to numerically model the flow of liquid in trapezoidal grooves using a finite difference approach in order to provide accurate information on the effects of cocurrent and countercurrent vapor flows on the pressure drop in the liquid. This geometry was chosen due to the fact that rectangular and triangular grooves are special cases of the trapezoidal groove, thus making the analysis as general as possible.

DiCola [1] solved the conservation of momentum equation for the laminar flow of liquid in rectangular grooves with a uniform shear stress imposed at the liquid–vapor interface using separation of variables. Unfortunately, this manuscript is no longer available in the open literature. Schneider and DeVos [2] provided the exact solution determined by DiCola [1], along with an expression for the friction factor which approximates the exact solution to within 1% by using the first term of the infinite series solution. This expression was used by Schneider and DeVos to determine the nondimensional heat transport capacity of axially grooved heat pipes. Upon examination of the DiCola equation, it is obvious that the rectangular groove is completely full, i.e., the meniscus contact angle is $\phi = 90°$.

Ayyaswamy et al. [3] used the Galerkin boundary method to solve the Poisson equation to determine the fluid velocity in triangular grooves. In this study, interfacial shear stress was zero, and the groove half-angle

* Corresponding author. Tel.: +1-937-775-5142; fax: +1-937-775-5009.

*E-mail address:* scott.thomas@wright.edu (S.K. Thomas).

[1] Currently with Belcan Corp.

0017-9310/01/$ - see front matter 
PII: S0017-9310(01)00007-2

**Nomenclature**

| | |
|---|---|
| $A_g$ | cross-sectional area of the groove, $m^2$ |
| $A_l$ | cross-sectional area of the liquid, $m^2$ |
| $A_{lv}$ | area of the liquid–vapor interface, $m^2$ |
| $A_w$ | area of the groove wall, $m^2$ |
| $A_l^*$ | $A_l/h^2$ |
| $\vec{a}_r$ | radial acceleration vector, $m/s^2$ |
| $\vec{A}$ | acceleration vector at any point in the helical groove, $m/s^2$ |
| $b$ | distance from the liquid–vapor interface to the bottom of the groove, m |
| $Bo$ | Bond number, $\rho g b^2/\sigma$ |
| $d^*$ | parameter defined in Eq. (4) |
| $D$ | diffusion coefficient |
| $D_h$ | hydraulic diameter, $4A_l/P$, m |
| $D_h^*$ | $D_h/h$ |
| $F_1$ | mean velocity parameter, $h_l^2\overline{v^*}$, $m^2$ |
| $F_2$ | volumetric flow rate parameter, $h_l^4\dot{V}^*$, $m^4$ |
| $f$ | friction coefficient, $2\overline{\tau_w}/\rho\bar{v}^2$ |
| $g$ | acceleration due to gravity, $m/s^2$ |
| $h$ | groove height, m |
| $h_{fg}$ | heat of vaporization, J/kg |
| $h_l$ | height of the liquid in the groove at the wall, m |
| $L_a$ | adiabatic length, m |
| $L_c$ | condenser length, m |
| $L_e$ | evaporator length, m |
| $L_{eff}$ | effective heat pipe length, $L_e/2 + L_a + L_c/2$, m |
| $L_p$ | pitch length, m |
| $L_t$ | total heat pipe length, m |
| $n$ | coordinate normal to the liquid–vapor interface |
| $n^*$ | $n/h$ |
| $N_g$ | number of grooves |
| $p$ | pressure, $N/m^2$ |
| $P$ | wetted perimeter, m |
| $P_{lv}$ | perimeter of the liquid–vapor interface, m |
| $P^*$ | $P/h$ |
| $P_{lv}^*$ | $P_{lv}/h$ |
| $Po$ | Poiseuille number, $fRe$ |
| $\dot{Q}_{cap}$ | capillary limit heat transport, W |
| $\dot{Q}_g$ | heat transfer due to a single groove, W |
| $\dot{Q}_t$ | total heat transported, $\sum_{i=1}^{N_g}\dot{Q}_{g,i}$, W |
| $R$ | radius of curvature of the liquid–vapor interface, m |
| $R_c$ | capillary radius, m |
| $R_h$ | radius of the helix, m |
| $R_v$ | radius of the heat pipe vapor space, m |
| $R^*$ | $R/h$ |
| $R_b^*$ | dimensionless radius of curvature at bifurcation |
| $Re$ | Reynolds number, $\rho\bar{v}D_h/\mu$ |
| $t$ | time, s |
| $T_{sat}$ | saturation temperature, K |
| $v$ | $y$-direction velocity, m/s |
| $\bar{v}$ | mean $y$-direction velocity, m/s |
| $\bar{v}_{l,max}$ | maximum mean liquid velocity, m/s |
| $\bar{v}_{v,max}$ | maximum mean vapor velocity, m/s |
| $v^*$ | $\mu v/h^2(-dp/dy)$ |
| $\overline{v^*}$ | dimensionless mean $y$-direction velocity |
| $\overline{v_0^*}$ | dimensionless mean $y$-direction velocity when $\tau_{lv}^* = 0$ |
| $\overline{v_a^*}$ | dimensionless mean $y$-direction velocity when $\tau_{lv}^* = \tau_{lv,a}^*$ |
| $v'$ | normalized mean velocity, $\overline{v^*}/\overline{v_0^*}$ |
| $V_g$ | total groove volume, $m^3$ |
| $V_l$ | liquid inventory volume, $m^3$ |
| $\dot{V}$ | volumetric flow rate, $\bar{v}A_l$, $m^3/s$ |
| $\dot{V}^*$ | $\mu\dot{V}/[h^4(-dp/dy)]$ |
| $w$ | width of the bottom of the groove, m |
| $w_l$ | width of the liquid in the groove, m |
| $x, y, z$ | coordinate directions |
| $x^*$ | $x/h$ |
| $z^*$ | $z/h$ |
| $\beta$ | groove aspect ratio, $w/2h$ |
| $\epsilon$ | convergence criterion |
| $\theta$ | groove half-angle, rad |
| $\mu$ | absolute viscosity, Pa-s |
| $\rho$ | density, $kg/m^3$ |
| $\sigma$ | surface tension, N/m |
| $\tau'$ | normalized shear stress at the liquid–vapor interface, $\tau_{lv}^*/\tau_{lv,0}^*$ |
| $\tau_{lv}$ | shear stress at the liquid–vapor interface, $N/m^2$ |
| $\tau_{lv}^*$ | $\tau_{lv}/h(-dp/dy)$ |
| $\tau_{lv,0}^*$ | shear stress at the liquid–vapor interface when $\overline{v^*} = 0$ |
| $\tau_{lv,a}^*$ | shear stress value in Fig. 9(a) |
| $\overline{\tau_w}$ | average shear stress at the wall, $N/m^2$ |
| $\overline{\tau_w^*}$ | $\overline{\tau_w}/h(-dp/dy)$ |
| $\phi$ | meniscus contact angle, rad |
| $\phi_0$ | minimum meniscus contact angle, rad |
| $\phi_b$ | meniscus contact angle at bifurcation, rad |

and contact angle were varied from $\theta = 5$–$60°$ and $\phi = 0.1°$ to the full groove condition ($\theta + \phi = 90°$). The results were presented graphically and in tabular form, which included the cross-sectional area, mean velocity, hydraulic diameter, and Poiseuille number. It was found that the Poiseuille number increased monotonically with meniscus contact angle.

Ma et al. [4] determined the Poiseuille number for the flow of liquid in triangular grooves with liquid–vapor frictional interaction. The groove half-angle ranged

from $20 \leqslant \theta \leqslant 60°$ and the meniscus contact angle was varied from $\phi = 0$–$60°$. The conservation of momentum equation was transformed into the Laplace equation in terms of liquid velocity, which was solved using separation of variables and linear superposition. Difficulties were encountered with respect to application of the liquid–vapor interface boundary condition, since the liquid–vapor interface velocity is an unknown function of the vapor velocity. The methodology used to overcome this difficulty required an experimentally determined coefficient. A dimensionless liquid–vapor interface flow number was introduced to account for the interfacial shear stress. This value determined the relative velocities of the liquid and vapor at the liquid–vapor interface, which impacted the magnitude of the Poiseuille number. It was found that the friction factor increased with the interface flow number and contact angle. Results from the experiment executed by Ayyaswamy et al. [3] for no liquid–vapor shear stress showed an excellent comparison with the analytical solution over the ranges of groove half-angle and contact angle mentioned above.

Peterson and Ma [5] performed a follow-up analysis to that of Ma et al. in which the Poiseuille number for flow in triangular grooves was determined using the Nachtsheim–Swigert iteration scheme and a numerical solution of a two-point boundary value problem. This allowed the velocity distributions in both the liquid and vapor to be solved as a coupled problem. Channel angles of $\theta = 10°$, $20°$, $30°$ and $40°$ and meniscus contact angles of $\phi = 0°$, $20°$, $40°$ and $60°$ were analyzed. It was determined that the dimensionless liquid–vapor flow number (previously defined by Ma et al.) was a function of the vapor velocity and the fluid properties of the liquid and vapor. An experiment was devised to validate the results of the numerical model. It was shown that increasing the countercurrent vapor flow increases the friction factor of the liquid. The agreement between the experimental data and the numerical model was quite good.

Romero and Yost [6] analyzed the flow of liquid in a triangular groove with no shear stress at the liquid–vapor interface. In particular, the flow from a sessile drop into the groove was of interest. A nonlinear partial differential diffusion equation was presented which described the time-dependent height of liquid in the groove in terms of the groove geometry, meniscus contact angle, and fluid properties. A simplified similarity solution was presented for the region which was far from the sessile drop. A full similarity solution was also shown which accounted for the region near the fluid droplet. It was found that the wetting front position was proportional to $(Dt)^{1/2}$, where the diffusion coefficient $D$ was related to the groove geometry, liquid viscosity, and liquid–vapor surface tension.

Lin and Faghri [7] modeled the flow of liquid in the triangular grooves of a rotating miniature heat pipe. A correlation for the friction factor was provided in terms of the shear stress at the liquid–vapor interface. The laminar flow in the triangular groove was solved using a finite element technique for side lengths ranging from $h\sqrt{1+\tan^2\theta} = 0.2$ to 0.65 mm and liquid–vapor shear stress $\tau_{lv} = 7.7 \times 10^{-5}$ to 0.055 N/m$^2$ for a groove half-angle of $\theta = 20°$ and meniscus contact angle $\phi = 30°$. A regression analysis was used to represent the data to within $\pm 2.8\%$.

Khrustalev and Faghri [8] analyzed the fully developed laminar flow of liquid and vapor in miniature heat pipes using a finite element solution. In particular, the case in which the vapor velocity was high and the cross-sectional areas of the vapor and liquid were comparable was of interest. It was assumed that, with respect to the vapor flow, the liquid velocity at the liquid–vapor interface was zero. For the liquid flow, the shear stress at the interface was equal and opposite to that of the vapor. This meant that the velocity gradient in the liquid was related to that of the vapor via a ratio of absolute viscosities. The momentum equation for the vapor domain was first solved to determine the shear stress distribution at the liquid–vapor interface. Then the momentum equation for the liquid domain was solved using the shear stress information from the vapor solution. The results presented were for a specific heat pipe geometry that matched a previous experimental study. It was found that the shear stress at the liquid–vapor interface was not uniform, being greater near the point of contact with the solid groove wall. This effect was more significant for smaller values of meniscus contact angle. In addition, the shear stress at the interface became more uniform as the vapor space became more restricted.

Kolodziej et al. [9] analyzed the gravity-driven flow of liquid in a triangular groove with no shear at the liquid–vapor interface. The shape of the liquid–vapor interface was determined in terms of the Bond number and meniscus contact angle. Starting with the Young–Laplace relation, a nonlinear boundary-value problem for the liquid–vapor interface shape was solved. The flow field was then solved for the friction factor using the boundary collocation method. The range of parameters was as follows: groove half-angle $\theta = 5°$ to $70°$, meniscus contact angle $\phi = 5°$ to $45°$, and Bond number $Bo = \rho g b^2/\sigma = 0.001$, 0.01, 0.1, 1.0 and 5.0, where $b$ is the vertical distance from the liquid–vapor interface to the bottom of the groove. It was found that the Bond number had a significant effect on the friction factor of the flow.

The objective of the present study was to determine the mean velocity, volumetric flow rate, and Poiseuille number for the flow of liquid in trapezoidal grooves. The effect of vapor flowing over the liquid–vapor interface was accounted for by relating the liquid velocity gradient to the friction factor of the vapor. This

approach assumed that the liquid velocity did not affect the vapor velocity; i.e., the vapor velocity at the interface was zero. In addition, the variation of the shear stress along the liquid–vapor interface was neglected [8]. The conservation of momentum equation was solved using Gauss–Seidel iteration with successive over-relaxation. The analysis was validated using the results of several previous studies including the flow of liquid in rectangular and triangular grooves with liquid–vapor interaction. The mean velocity, volumetric flow rate, and Poiseuille number are presented in terms of the groove aspect ratio ($0 \leqslant \beta \leqslant 1.5$), groove half-angle ($0 \leqslant \theta \leqslant 60°$), meniscus contact angle ($0 \leqslant \phi \leqslant 90° - \theta$), and dimensionless shear stress at the liquid–vapor interface ($-0.45 \leqslant \tau^*_{lv} \leqslant 5.0$). The results were used to determine the effects of groove fill amount on the capillary limit of the revolving helically grooved heat pipe studied by Castle et al. [10]. The predictions of the improved capillary limit model were compared to the experimental data obtained.

## 2. Mathematical model

A constant property liquid flows steadily in a trapezoidal groove as shown in Fig. 1. A meniscus, which is assumed to be circular, comprises the liquid–vapor interface. For fully developed laminar flow with no body forces, the dimensionless conservation of mass and momentum equations reduce to [11]

$$\frac{\partial^2 v^*}{\partial x^{*2}} + \frac{\partial^2 v^*}{\partial z^{*2}} = -1. \tag{1}$$

On the groove walls, the no-slip condition is in effect.

$$v^* = 0 : \begin{cases} 0 \leqslant x^* \leqslant \beta, \;\; z^* = 0, \\ \beta \leqslant x^* \leqslant \beta + \tan\theta, \;\; z^* = (x^* - \beta)\cot\theta \;\; \text{for } \theta > 0, \\ x^* = \beta, \;\; 0 \leqslant z^* \leqslant 1 \;\; \text{for } \theta = 0. \end{cases} \tag{2}$$

At the line of symmetry, the velocity gradient is zero in the $x^*$ direction

$$\frac{\partial v^*}{\partial x^*} = 0 : \quad x^* = 0, \quad 0 \leqslant z^* \leqslant (1 + d^*) - R^*, \tag{3}$$

where

$$d^* = R^* \sqrt{1 - \left( \frac{\beta + \tan\theta}{R^*} \right)^2}. \tag{4}$$

The dimensionless radius of curvature is given by

$$R^* = \begin{cases} (\beta + \tan\theta) \sqrt{1 + \left[ \cot\theta - \dfrac{\sin\phi}{\sin\theta \sin(\theta + \phi)} \right]^{-2}} & \text{for } \theta > 0 \\ \beta \sec\phi \;\; \text{for } \theta = 0. \end{cases} \tag{5}$$

On the liquid–vapor interface, a uniform shear stress in the $y$ direction is imposed.

$$\frac{\partial v^*}{\partial n^*} = \tau^*_{lv} : \;\; 0 \leqslant x^* \leqslant \beta + \tan\theta, \quad z^* = (1 + d^*) - \sqrt{R^{*2} - x^{*2}}. \tag{6}$$

The dimensional liquid–vapor interface shear stress can be cast in terms of the friction factor of the vapor.

$$\tau_{lv} = \begin{cases} \left[ \dfrac{\rho_v (\overline{v}_v)^2}{2} \right] f_v & \text{for cocurrent flow,} \\ -\left[ \dfrac{\rho_v (\overline{v}_v)^2}{2} \right] f_v & \text{for countercurrent flow.} \end{cases} \tag{7}$$

The Poiseuille number of the liquid in the groove is given by

$$Po = fRe = \frac{D^{*2}_h}{2\overline{v}^*}. \tag{8}$$

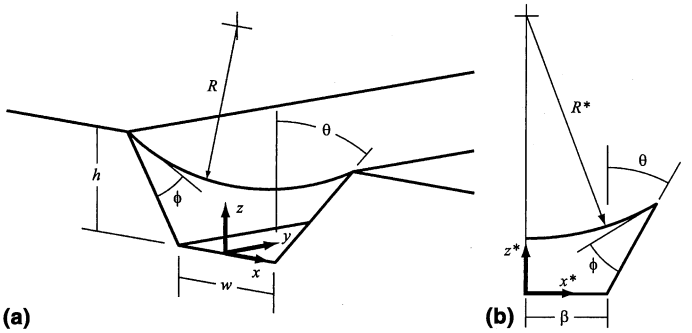


Fig. 1. Flow of liquid in a trapezoidal groove: (a) coordinate system; (b) solution domain.

The dimensionless hydraulic diameter is

$$D_h^* = \begin{cases} 2\left[\beta + (\beta + \tan\theta)(1 + d^*) - R^{*2}\cos^{-1}\left(\dfrac{d^*}{R^*}\right)\right] \\ \quad \times(\beta + \sec\theta)^{-1} \quad \text{for } \theta + \phi < \pi/2 \\ 2(2\beta + \tan\theta)(\beta + \sec\theta)^{-1} \quad \text{for } \theta + \phi = \pi/2. \end{cases} \tag{9}$$

The mean velocity is defined as

$$\overline{v^*} = \frac{2}{A_l^*}\int_0^{\beta+\tan\theta}\int_0^{z^*} v^*\,dz^*\,dx^*, \tag{10}$$

where the dimensionless cross-sectional area is given by

$$A_l^* = \begin{cases} \beta + (\beta + \tan\theta)(1 + d^*) - R^{*2}\cos^{-1}\left(\dfrac{d^*}{R^*}\right) \\ \quad \text{for } \theta + \phi < \pi/2, \\ 2\beta + \tan\theta \quad \text{for } \theta + \phi = \pi/2. \end{cases} \tag{11}$$

## 3. Numerical model

The elliptic Poisson equation given in Eq. (1) with mixed boundary conditions (Eqs. (2), (3), and (6)) was solved using Gauss–Seidel iteration with successive over-relaxation and a central differencing scheme [12]. The convergence criteria for the iterative solution were set to $\epsilon = 10^{-8}$ for each case. A grid independence check was made in which the number of grids in each direction was doubled. When the value for the Poiseuille number did not change by more than 3%, grid independence was considered to be reached. The convergence criterion was then reduced by an order of magnitude while maintaining the highest number of grids. If the Poiseuille number did not change by more than 2%, the solution was considered to be independent of both grid size and $\epsilon$. Otherwise, a grid independence check was made at the smaller value of $\epsilon$ until a converged solution was obtained. In fact, the grid independence for 423 of the 446 data points reported was less than 1% [13].

The numerical model was tested against several existing solutions, such as rectangular ducts, triangular grooves without interfacial shear stress, and rectangular and triangular grooves with shear stress. See Lykins [13] for details.

Shah [14] determined the friction factors for the laminar flow within ducts of various cross-sections using a least-squares-matching technique. A comparison was made of the Poiseuille number between the present solution and those given by Shah [14] and Shah and London [15] for laminar flow in a family of rectangular ducts ($\theta = 0°$, $0.01 \leqslant \beta \leqslant 1.0$). The agreement was excellent, with a maximum difference of 0.9%.

Ayyaswamy et al. [3] presented the friction factors obtained for laminar flow in triangular grooves using the Galerkin method of solution. Romero and Yost [6] derived an equation for the dimensionless volumetric flow rate of liquid in a triangular groove using asymptotic methods and a regression analysis. Kolodziej et al. [9] used the boundary collocation method to solve the same problem, except that the liquid–vapor interface was not assumed to be circular. The present solution was compared to that obtained by Ayyaswamy et al. for $\theta = 5°$ and 60° for the full range of meniscus contact angle ($0.1° \leqslant \phi \leqslant 90° - \theta$). The agreement was excellent for $\theta = 60°$, but was less so for $\theta = 5°$. This was due to the extreme narrowness of the flow field for this case. The maximum percent differences for $\theta = 5°$ and 60° were 3.7% and 0.9%, respectively. In comparison to the results by Romero and Yost [6], the maximum percent differences were 2.2% for $\theta = 5°$ and 2.3% for $\theta = 60°$. The agreement with the results provided by Kolodziej et al. for the lowest value of Bond number presented ($Bo = 0.001$) was less satisfactory, with a maximum percent difference of 4.5% for $\theta = 5°$, and 19.9% for $\theta = 60°$. This may be due to the approximate nature of the solution by Kolodziej et al., which was in terms of a truncated infinite summation.

DiCola [1] presented the solution for the Poiseuille number for the laminar flow of a constant property fluid within a rectangular groove. While interfacial shear stress at the liquid–vapor interface was accounted for, the groove was assumed to be completely full, with a meniscus contact angle of $\phi = 90°$. The comparison between the equation by DiCola and the results of the present analysis for laminar flow in a family of rectangular grooves at the full groove condition ($\phi = 90°$, $0.1 \leqslant \beta \leqslant 1.0$, $\tau_{lv}^* = -0.1$, 0.0, and 1.0) resulted in an excellent agreement with a maximum percent difference of 2.3%.

The present model was compared to the correlation presented by Lin and Faghri [7], where the friction factor for the flow of liquid in triangular grooves with liquid–vapor shear was presented. Unfortunately, not enough information was provided by Lin and Faghri to precisely determine the limits of applicability for their equation. Therefore, the correlation was evaluated over a fairly wide range for comparison with the present solution. The agreement was quite good between $0.075 \leqslant -\tau_{lv}^* \leqslant 0.1$, where the maximum percent difference in this range was 2.2%.

## 4. Results and discussion

### 4.1. Parametric analysis

A numerical study has been completed in which the flow field in a trapezoidal groove has been solved. Specifically, values of the mean velocity, Poiseuille number, and volumetric flow rate are reported for various values of the groove aspect ratio, groove half-angle,

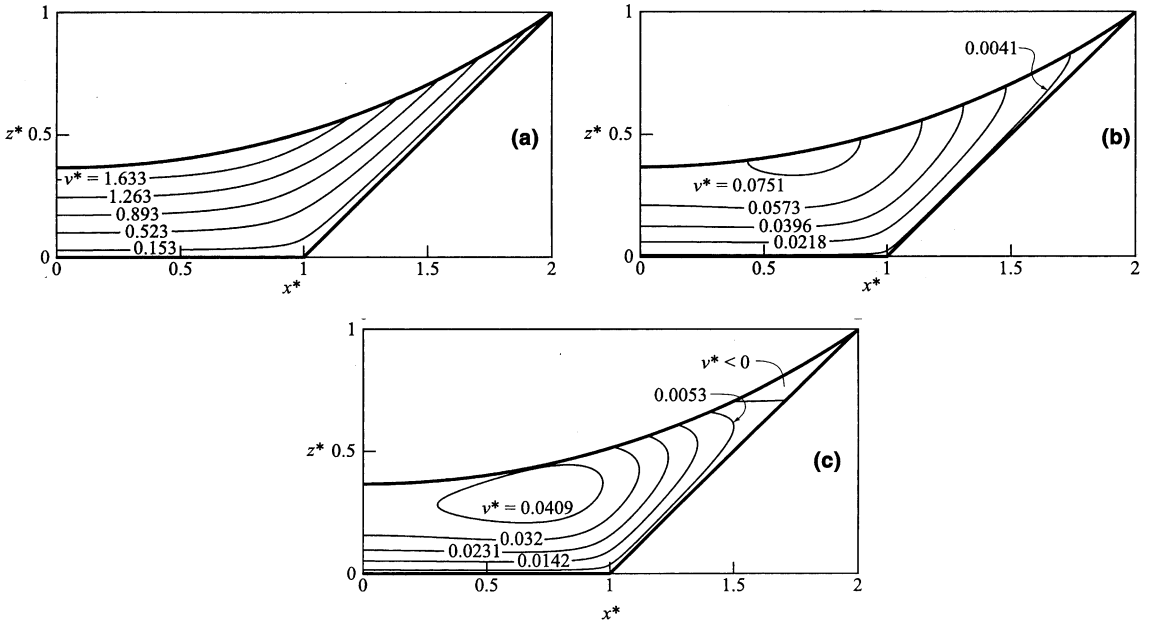


Fig. 2. Dimensionless velocity fields for laminar flow in trapezoidal grooves ($\beta = 1.0$, $\phi = 10°$, $\theta = 45°$): (a) $\tau^*_{lv} = 5.0$ (cocurrent flow); (b) $\tau^*_{lv} = 0.0$; (c) $\tau^*_{lv} = -0.1$ (countercurrent flow).

meniscus contact angle, and dimensionless shear stress at the liquid–vapor interface. Fig. 2 shows a contour plot of the dimensionless mean velocity obtained for cocurrent flow, no shear stress, and countercurrent flow. The flow behavior changes significantly with shear stress, where the maximum velocity is located along the liquid–vapor interface for $\tau^*_{lv} = 5.0$ and 0.0, and within the interior of the flow field for $\tau^*_{lv} = -0.1$. For countercurrent flow (Fig. 2(c)), a region of reversed flow occurs near the intersection of the groove wall and the liquid–vapor interface. Depending on the magnitude of the countercurrent shear stress, the liquid velocity could be entirely reversed.

Fig. 3 presents the mean velocity versus shear stress at the liquid–vapor interface for several values of the groove half-angle. The range of the meniscus contact angle $(0 \leqslant \phi \leqslant 90° - \theta)$ was divided equally to show the behavior of the mean velocity with $\phi$. The mean velocity increases linearly with shear stress since the flow is aided by $\tau^*_{lv}$. In addition, $\overline{v^*}$ increases with groove half-angle and meniscus contact angle, which is a result of an increase in cross-sectional area. As the groove half-angle $\theta$ increases, $\overline{v^*}$ becomes more sensitive to the meniscus contact angle $\phi$ due to the increased length of the perimeter of the liquid–vapor interface.

Fig. 4 shows that the Poiseuille number decreases dramatically as the shear stress at the liquid–vapor interface increases. For countercurrent flow $(\tau^*_{lv} < 0)$, the Poiseuille number is a strong function of shear stress since the mean velocity approaches zero. In addition, the Poiseuille number decreases with increasing meniscus contact angle for a given value of shear stress. For cocurrent flow $(\tau^*_{lv} > 0)$, the Poiseuille number is a lesser function of the shear stress, but increases significantly with meniscus contact angle. The Poiseuille number is a weak function of the groove half-angle.

The volumetric flow rate versus shear stress for various meniscus contact angles can be seen in Fig. 5. The volumetric flow rate and mean velocity display similar trends. The volumetric flow rate is a linear function of shear stress, and increases with meniscus contact angle and groove half-angle. The flow rate is slightly more sensitive than the mean velocity with respect to the meniscus contact angle. The mean velocity is given as a function of the interfacial shear stress for a constant meniscus contact angle in Fig. 6. For $\theta = 0$ and 30°, the mean velocity increases and then decreases with groove aspect ratio. This point can be further elucidated in Fig. 7, which presents the mean velocity, Poiseuille number and volumetric flow rate for $\phi = 30°$ and $\tau^*_{lv} = 5.0$. As mentioned previously, the mean velocity increases and then decreases with $\beta$ for $\theta \leqslant 30°$. This phenomenon also impacts the Poiseuille number and the volumetric flow rate, where $\dot{V}^*$ attains a maximum value with respect to $\beta$ for a given groove half-angle $\theta \leqslant 15°$. Fig. 8 shows $\overline{v^*}$, $Po$, and $\dot{V}^*$ versus $\theta$ for $\beta = 1.0$ and $\tau^*_{lv} = 5.0$. In general, these functions increase significantly with both meniscus contact angle

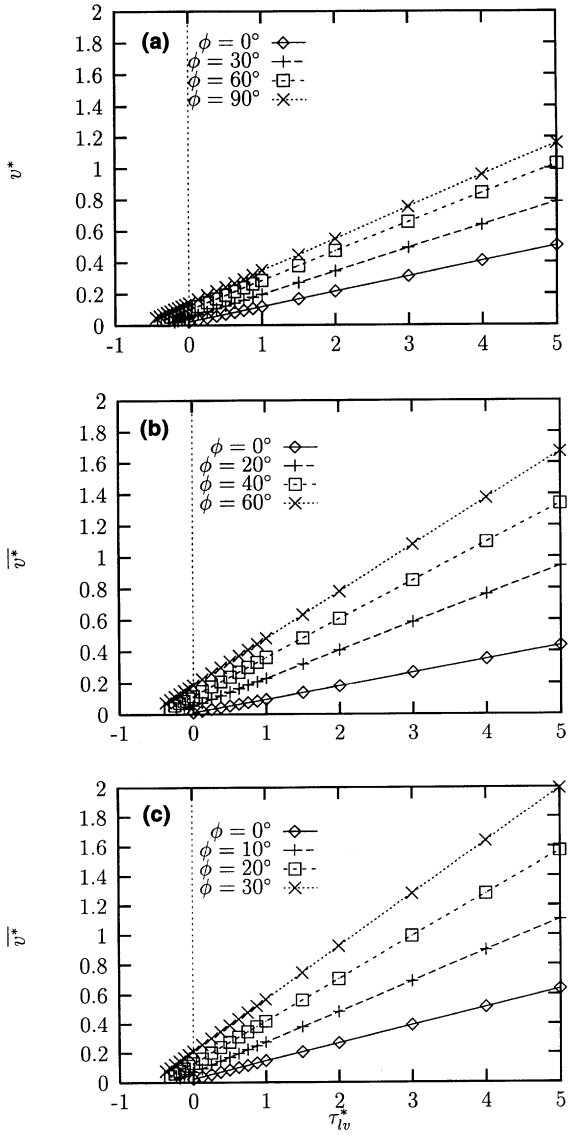


Fig. 3. $\overline{v^*}$ versus $\tau^*_{\mathrm{lv}}$ for laminar flow in trapezoidal grooves ($\beta = 1.0$): (a) $\theta = 0°$; (b) $\theta = 30°$; (c) $\theta = 60°$.

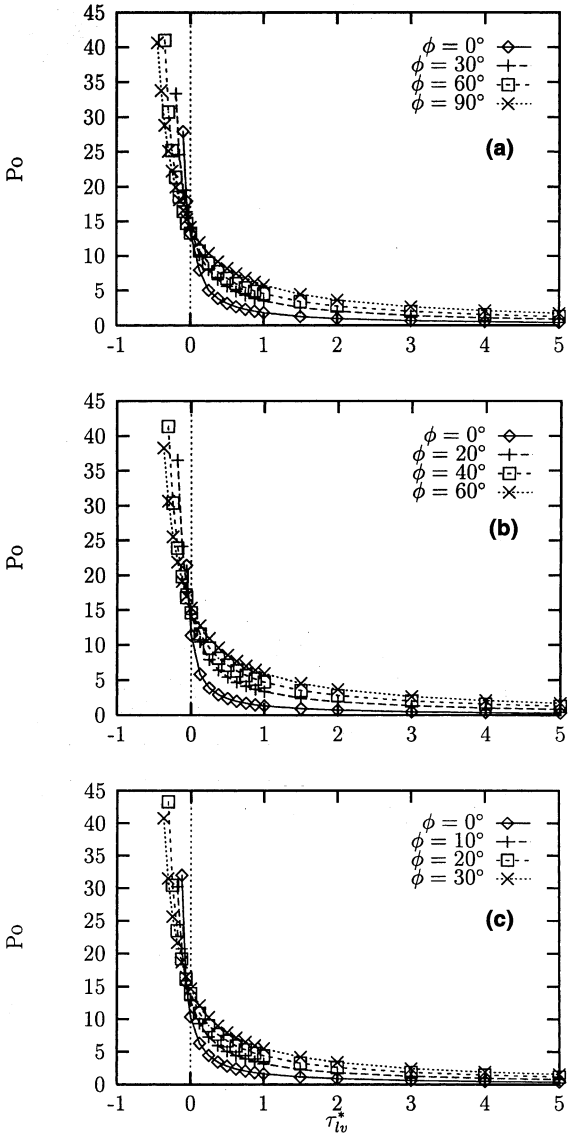


Fig. 4. *Po* versus $\tau^*_{\mathrm{lv}}$ for laminar flow in trapezoidal grooves ($\beta = 1.0$): (a) $\theta = 0°$; (b) $\theta = 30°$; (c) $\theta = 60°$.

and groove half-angle, except for the Poiseuille number for $\theta = 0°$ and $\phi \leqslant 20°$.

### 4.2. Semi-analytical and two-point numerical solutions for $\overline{v^*}$

As seen in Figs. 3 and 6, the mean velocity is a linear function of the imposed shear stress at the liquid–vapor interface. Since a direct numerical simulation of the liquid flow field for a number of values of the shear stress is computer resource intensive, it is appropriate to seek a semi-analytical expression for $\overline{v^*}$. Fig. 9(a) shows the definition of the parameters involved, where the mean velocity when the shear stress is zero $(0, \overline{v_0^*})$ is given by the numerical solution. The value for the liquid–vapor shear for which the mean velocity is zero $(\tau^*_{\mathrm{lv},0}, 0)$ is given by the following force balance analysis. Fig. 9(b) shows a differential element of the liquid in the groove. A force balance between the pressure drop and the shear forces at the liquid–vapor interface and at the wall results in the following relation:

$$p_y A_{\mathrm{l}} - p_{y+\mathrm{d}y} A_{\mathrm{l}} + \tau_{\mathrm{lv}} A_{\mathrm{lv}} - \overline{\tau_{\mathrm{w}}} A_{\mathrm{w}} = 0. \tag{12}$$

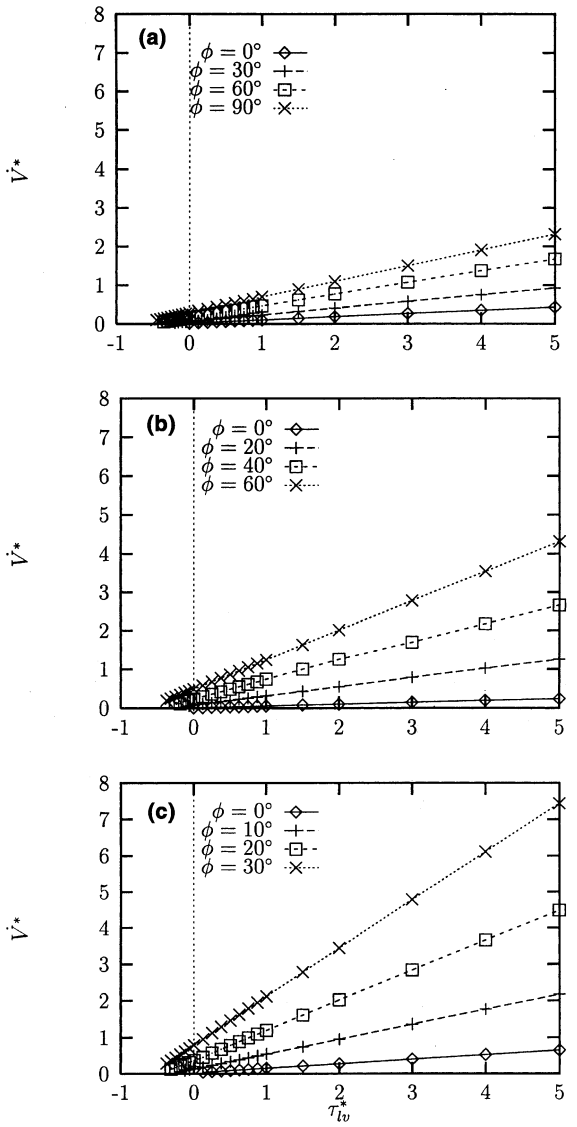


Fig. 5. $\dot{V}^*$ versus $\tau^*_{\mathrm{lv}}$ for laminar flow in trapezoidal grooves ($\beta = 1.0$): (a) $\theta = 0°$; (b) $\theta = 30°$; (c) $\theta = 60°$.

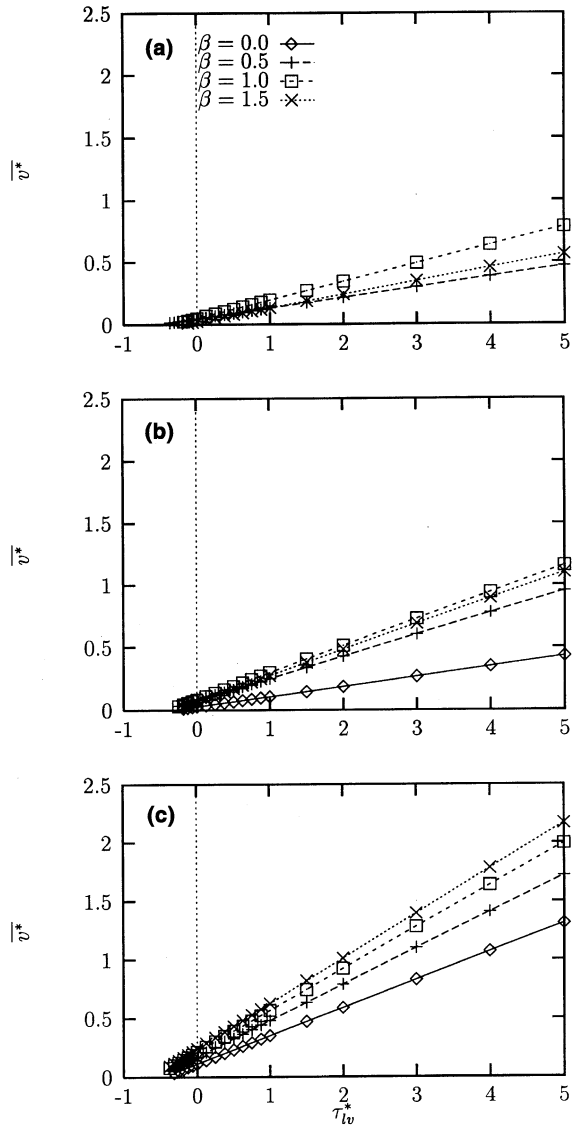


Fig. 6. $\overline{v^*}$ versus $\tau^*_{\mathrm{lv}}$ for laminar flow in trapezoidal grooves ($\phi = 30°$): (a) $\theta = 0°$; (b) $\theta = 30°$; (c) $\theta = 60°$.

The areas over which the shear stresses $\tau_{\mathrm{lv}}$ and $\overline{\tau_{\mathrm{w}}}$ act are $A_{\mathrm{lv}} = P_{\mathrm{lv}}\,\mathrm{d}y$ and $A_{\mathrm{w}} = P\,\mathrm{d}y$, respectively. Using these areas and nondimensionalizing gives

$$A^*_{\mathrm{l}} + \tau^*_{\mathrm{lv}} P^*_{\mathrm{lv}} - \overline{\tau^*_{\mathrm{w}}} P^* = 0. \tag{13}$$

For Poiseuille flow in ducts of arbitrary cross-section, and combined Couette–Poiseuille flow between flat plates, the shear stress at the wall is related to the mean velocity of the fluid by a constant [11]. In the present analysis, it is assumed that this also holds for the flow of liquid in a trapezoidal groove with an imposed shear stress at the liquid–vapor interface.

$$\overline{\tau^*_{\mathrm{w}}} = C_1 \overline{v^*}. \tag{14}$$

It should be noted that the constant $C_1$ is probably a function of the groove geometry and meniscus contact angle. However, since the objective of this analysis is to determine the liquid–vapor shear stress when the mean liquid velocity is zero, this functionality is unimportant.

Substituting this relation into the force balance equation results in the following expression for mean velocity

$$\overline{v^*} = \frac{1}{C_1 P^*}\left(A^*_{\mathrm{l}} + \tau^*_{\mathrm{lv}} P^*_{\mathrm{lv}}\right), \tag{15}$$

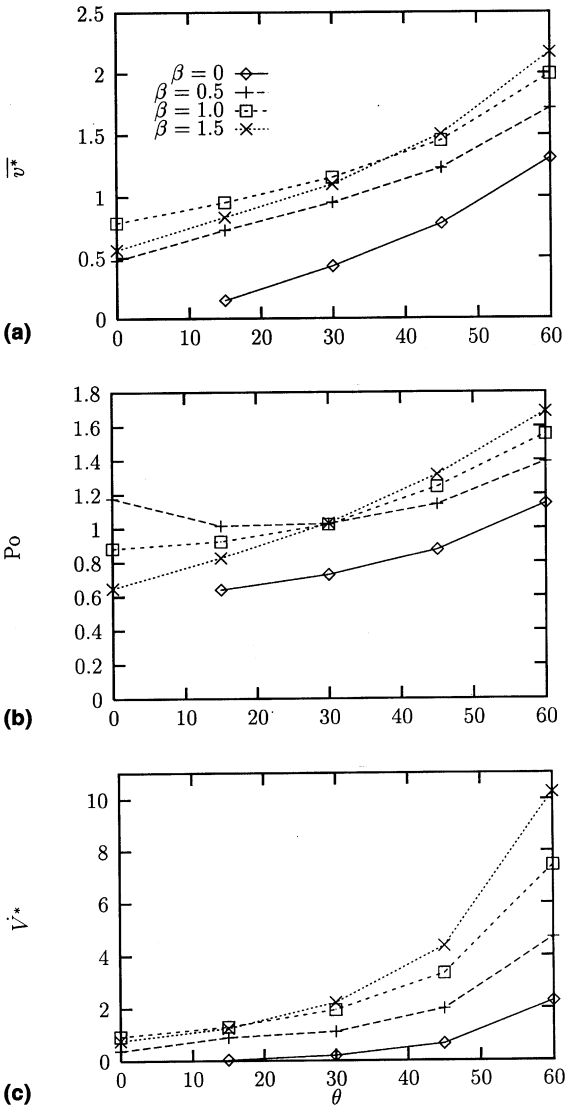


Fig. 7. $\overline{v^*}$, *Po* and $\dot{V}^*$ versus $\theta$ for laminar flow in trapezoidal grooves ($\phi = 30°$, $\tau^*_{lv} = 5.0$).

where the perimeter of the liquid–vapor interface is

$$P^*_{lv} = \begin{cases} 2R^* \sin^{-1}\left(\dfrac{\beta + \tan\theta}{R^*}\right) & \text{for } \theta + \phi < \pi/2, \\ 2(\beta + \tan\theta) & \text{for } \theta + \phi = \pi/2. \end{cases} \tag{16}$$

The mean velocity is zero when the shear stress at the liquid–vapor interface is

$$\tau^*_{lv,0} = -\frac{A^*_l}{P^*_{lv}}. \tag{17}$$

Figs. 10(a) and (b) show the results of Eq. (17). The numerical results shown in Figs. 3 and 6 were extrapolated to determine the values for shear stress at the liquid–vapor interface when $\overline{v^*} = 0$. The prediction given by Eq. (17) is quite good given the simplicity of the closed-form solution. The equation for the normalized mean velocity as a function of the shear stress is given by

$$v' = \overline{v^*}/\overline{v^*_0} = 1 - \tau', \tag{18}$$

where $\tau' = \tau^*_{lv}/\tau^*_{lv,0}$. The semi-analytical solution for the normalized mean velocity is shown in Fig. 10(c) with the corresponding numerical data presented in Figs. 3 and 6. Eq. (18) predicts 93% of the data to within ±30% over the range of the meniscus contact angle, groove half-angle, groove aspect ratio and liquid–vapor shear stress examined in Figs. 3 and 6.

The two-point numerical solution of $\overline{v^*}$ as a function of $\tau^*_{lv}$ is also shown in Fig. 9(a). The finite difference numerical model is used to compute the mean velocity for two values of liquid–vapor shear stress [$(0, \overline{v^*_0})$ and $(\tau^*_{lv,a}, \overline{v^*_a})$]. The equation for the normalized mean velocity as a function of shear stress using this solution is given by Eq. (18), and the shear stress when the mean velocity is zero is

$$\tau^*_{lv,0} = \frac{\tau^*_{lv,a}}{(1 - \overline{v^*_a}/\overline{v^*_0})}. \tag{19}$$

### 4.3. Effect of groove fill ratio

Fig. 11(a) shows the case when liquid evaporates from a trapezoidal groove. Initially, the groove is full with $\phi + \theta = 90°$. The contact angle decreases until the minimum meniscus contact angle $\phi_0$ for the particular solid–liquid combination is reached. Past this point, the meniscus detaches from the top of the groove and recedes until the lowest part of the meniscus reaches the bottom of the groove [16]. When the thickness of the liquid film at the bottom of the groove is on the order of several hundred Angstroms, forces due to London–van der Waals interactions with the surrounding liquid and solid molecules induce instabilities in the fluid [17]. These instabilities cause the liquid in the groove to bifurcate into two separate flows in the corners of the groove, which are each equivalent to the flow in a triangular groove. The liquid in the two corners of the groove will continue to recede until it is depleted.

The dimensions of the grooves analyzed by Castle et al. [10] were used to determine the volumetric flow rate of ethanol in a trapezoidal copper groove as a function of the amount of liquid in the groove. The geometric values of the parametric analysis depicted in Fig. 11(a) are given by Lykins [13]. Faghri [18] gives

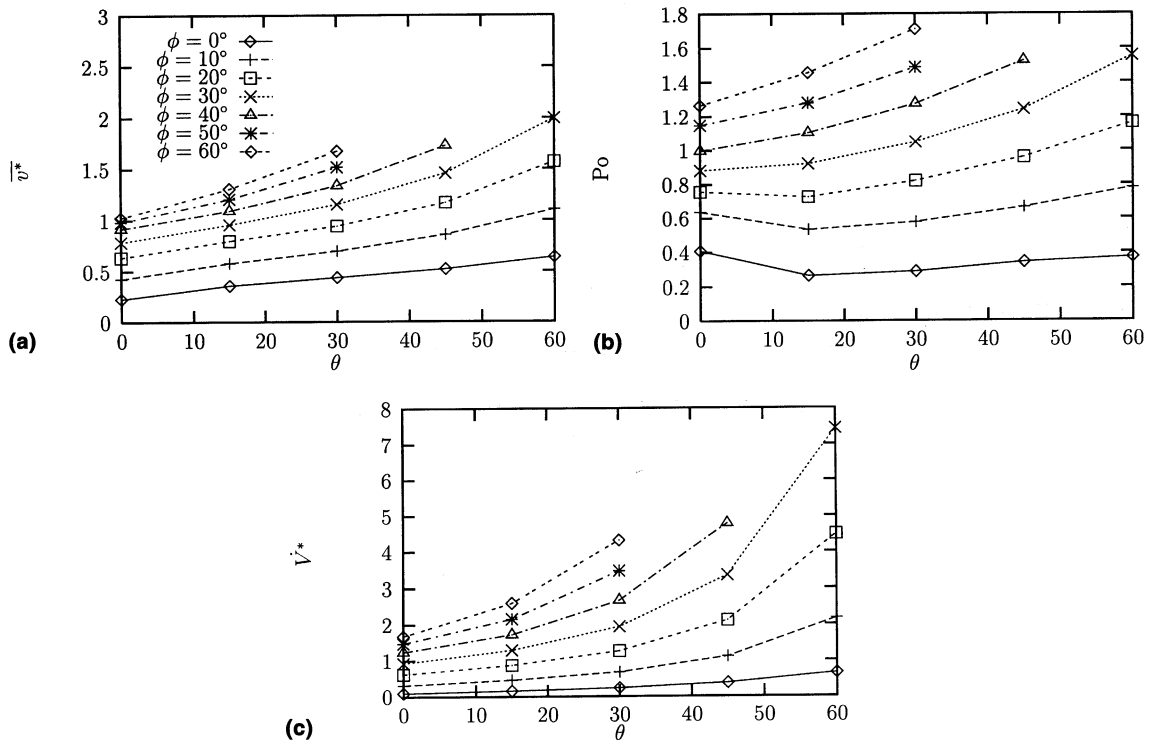


Fig. 8. $\overline{v^*}$, *Po* and $\dot{V}^*$ versus $\theta$ for laminar flow in trapezoidal grooves ($\beta = 1.0$, $\tau^*_{\mathrm{lv}} = 5.0$).

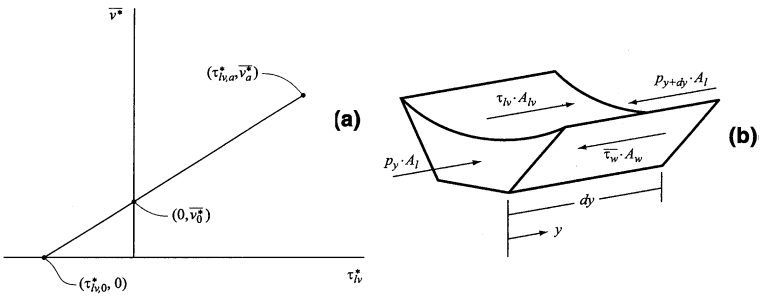


Fig. 9. Semi-analytical and two-point numerical solutions for $\overline{v^*}$: (a) definition of parameters; (b) force balance on the liquid in a trapezoidal groove.

$\phi_0 = 7°$ for a receding meniscus of ethanol on copper. In terms of the present analysis, as the liquid recedes into the groove, the groove aspect ratio $\beta$ increases. In addition, after bifurcation occurs $\beta = 0$, and the groove half-angle $\theta$ changes to that of the corner of the groove. A relation for the point at which bifurcation occurs is provided where the liquid is assumed to bifurcate when the lowest part of the meniscus actually reaches the bottom of the groove. The radius of curvature at the bifurcation point for a trapezoidal groove is

$$R^*_{\mathrm{b}} = \frac{1}{2}[1 + (\beta + \tan\theta)^2]. \tag{20}$$

The meniscus contact angle at bifurcation as a function of the groove geometry is

$$\phi_b = \tan^{-1}\left(\frac{1}{\sin\theta}\left\{\left[\cos\theta + \frac{2\sin\theta(\beta+\tan\theta)}{1-(\beta+\tan\theta)^2}\right]^{-1} - \cos\theta\right\}\right)^{-1}. \tag{21}$$

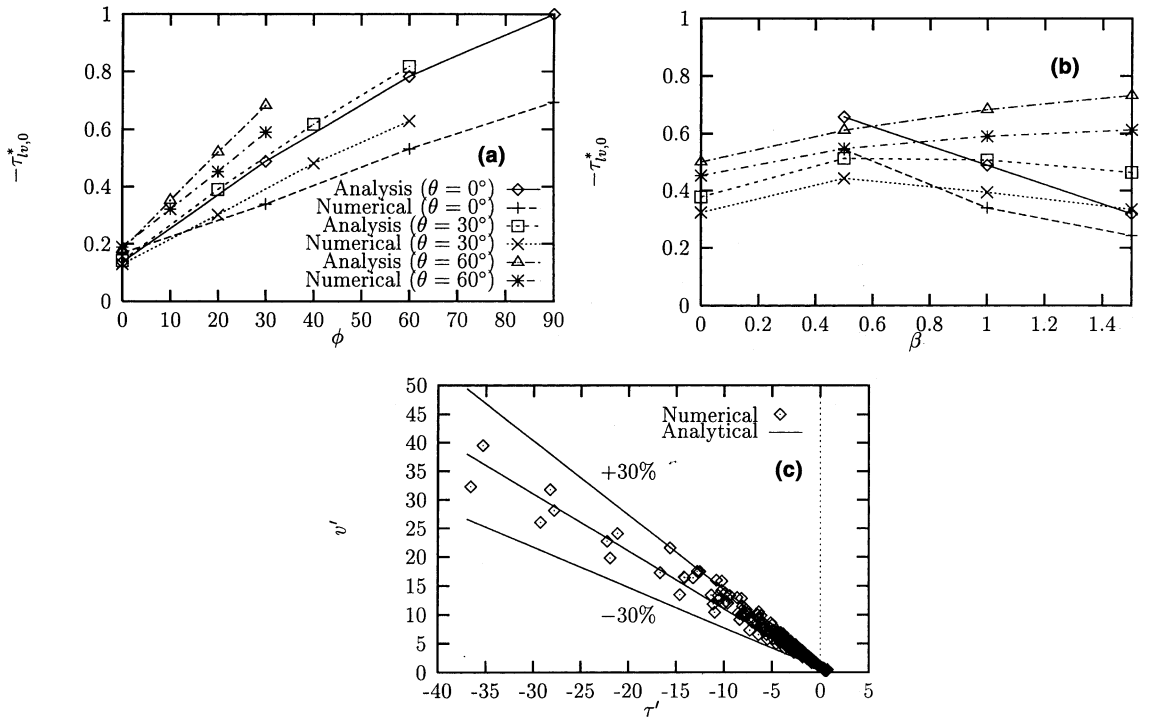


Fig. 10. Numerical and semi-analytical solution comparison: (a) $-\tau^*_{lv,0}$ versus $\phi$ for $\beta = 1.0$ (from Fig. 3); (b) $-\tau^*_{lv,0}$ versus $\beta$ for $\phi = 30°$ (from Fig. 6); (c) normalized mean velocity versus normalized shear stress at the liquid–vapor interface (from Figs. 3 and 6).

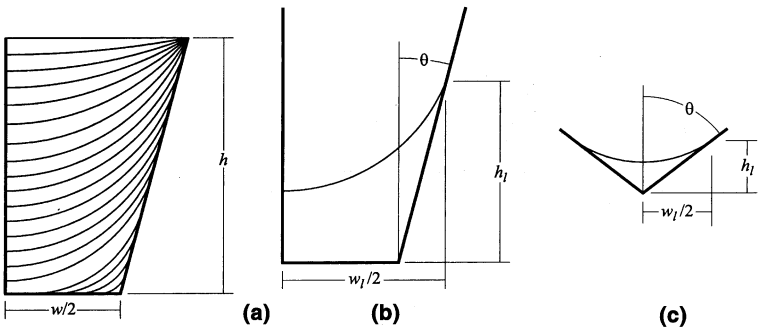


Fig. 11. Effect of groove fill ratio on liquid flowing in a trapezoidal groove: (a) parametric analysis (to scale, $h = 0.03831$ cm, $w = 0.03445$ cm, $\theta = 14.62°$); (b) definition of variables prior to bifurcation of the liquid; (c) definition of variables after bifurcation of the liquid.

The radius of curvature of the liquid–vapor interface is shown in Fig. 12(a) as a function of the groove fill ratio. When the groove is nearly full, the radius of curvature approaches infinity. As the amount of liquid in the groove decreases, the radius of curvature is relatively constant, and then becomes very small after the liquid bifurcates into the corners of the groove. Figs. 12(b) and (c) show two flow parameters, $F_1$ and $F_2$, which allow the presentation of the mean velocity and volumetric flow rate before and after bifurcation on the same graph. Both flow parameters increase monotonically with groove fill ratio, as expected. In Fig. 12(c), for a groove fill ratio of $A_l/A_g = 0.158$, the volumetric flow rate was 1% of that for the full groove due to the decrease in flow area. This figure shows that the groove was

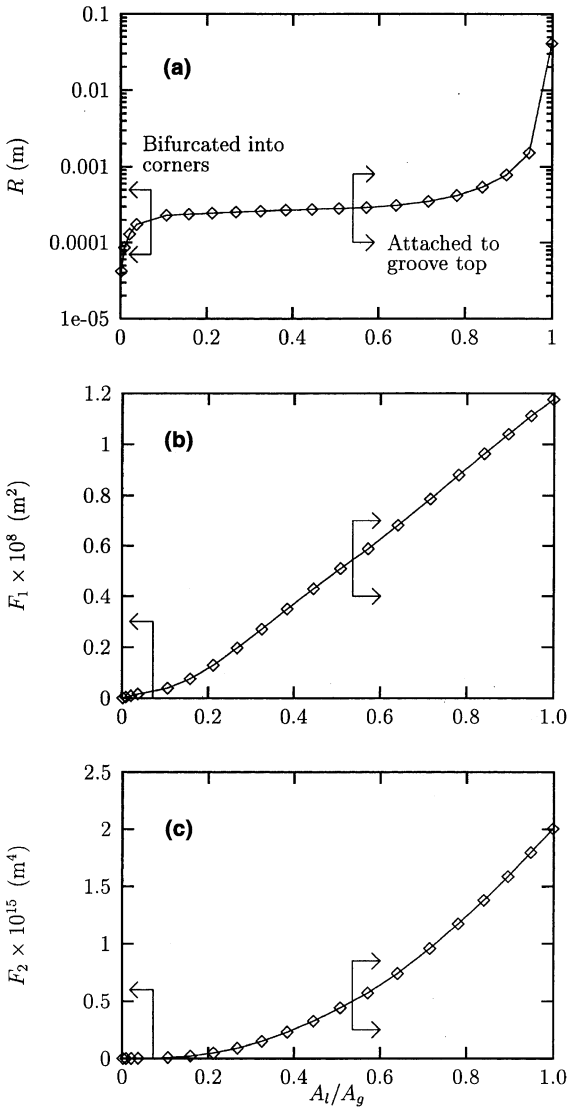


Fig. 12. Effect of groove fill ratio: (a) radius of curvature of the liquid–vapor interface; (b) mean velocity parameter; (c) volumetric flow rate parameter.

essentially shut off for $A_l/A_g \leqslant 0.158$, which was prior to bifurcation. Using the functional relationship for mean velocity given by Eq. (15), the volumetric flow rate is

$$\dot{V}^* = \frac{A_l^*}{C_l P^*}(A_l^* + \tau_{lv}^* P_{lv}^*). \tag{22}$$

When $\tau_{lv}^* = 0$, $\dot{V} \propto A_l^2$, which confirms that the volumetric flow rate should decrease rapidly with decreasing flow area for $A_l < 1$.

### 4.4. Capillary limit analysis for a revolving helically grooved heat pipe

Using the results of the numerical analysis, the capillary limit prediction for a revolving helically grooved heat pipe proposed by Thomas et al. [19] was improved by accounting for the effects of working fluid fill amount and the shear stress at the liquid–vapor interface. The improved model was compared to the experimental data collected by Castle et al. [10], who determined the capillary limit of a revolving helically grooved copper–ethanol heat pipe for radial accelerations of $|\vec{a_r}| = 0.01$, 2.0, 4.0, 6.0, 8.0 and 10.0-g and groove fill ratios of $V_l/V_g = 0.5$, 1.0 and 1.5. The dimensions of the heat pipe examined by Castle et al. [10] are given in Table 1. A pressure balance within the heat pipe results in the following expression for the capillary limit [18,20]:

$$\Delta p_{cap,max} \geqslant \Delta p_v + \Delta p_l + \Delta p_{bf}. \tag{23}$$

The maximum capillary pressure for an axial groove is

$$\Delta p_{cap,max} = \frac{\sigma}{R_c}. \tag{24}$$

It is assumed that the capillary limit occurs when the liquid bifurcates into the corners of the grooves. This statement is based on the results of the variation of the volumetric flow rate with groove fill ratio in Fig. 12. The capillary radius when the liquid bifurcates ($R_c = 0.02252$ cm) was found using Eqs. (20) and (21).

For a circular cross-section heat pipe with uniform heat input and output along the lengths of the evaporator and condenser, respectively, the pressure drop in the vapor is

$$\Delta p_v = \frac{8\mu_v L_{eff}\dot{Q}_t}{\pi \rho_v h_{fg} R_v^4}. \tag{25}$$

Table 1
Specifications of the heat pipe test article examined by Castle et al. [10]

| | |
|---|---|
| Groove height, $h$ | 0.03831 cm |
| Groove base width, $w$ | 0.03445 cm |
| Groove half-angle, $\theta$ | 14.62° |
| Evaporator length, $L_e$ | 15.2 cm |
| Adiabatic length, $L_a$ | 8.2 cm |
| Condenser length, $L_c$ | 15.2 cm |
| Vapor space radius, $R_v$ | 0.6795 cm |
| Number of grooves, $N_g$ | 50 |
| Helical pitch length, $L_p$ | 135.8 cm |
| Helix radius, $R_h$ | 0.6992 cm |

The pressure drop in the liquid was found by using the normalized mean velocity relation (Eq. (18)) rewritten in dimensional form.

$$\mathrm{d}p_\mathrm{l} = -\left(\frac{\mu_\mathrm{l}\overline{v_\mathrm{l}}}{h_\mathrm{l}^2\overline{v_0^*}} + \frac{\tau_\mathrm{lv}}{h_\mathrm{l}\tau_{\mathrm{lv},0}^*}\right)\mathrm{d}y. \tag{26}$$

In a heat pipe, the liquid flows opposite to the vapor in all regions. Therefore, the shear stress at the liquid–vapor interface for countercurrent flow was used (Eq. (7)). The Poiseuille number of the vapor flow was modeled as laminar flow within a smooth tube with a circular cross-section ($Po_\mathrm{v} = 16$). Substituting these relations into Eq. (26) gives

$$\mathrm{d}p_\mathrm{l} = -\left(\frac{\mu_\mathrm{l}\overline{v_\mathrm{l}}}{h_\mathrm{l}^2\overline{v_0^*}} - \frac{4\mu_\mathrm{v}\overline{v_\mathrm{v}}}{h_\mathrm{l}R_\mathrm{v}\tau_{\mathrm{lv},0}^*}\right)\mathrm{d}y. \tag{27}$$

It is assumed that the cross-sectional area of the liquid is constant along the length of the groove. For a constant heat flux in both the evaporator and condenser sections, Eq. (27) can be integrated to determine the total pressure drop in the helical groove.

$$\Delta p_\mathrm{l} = L_\mathrm{eff}\left(\frac{\mu_\mathrm{l}\overline{v}_{\mathrm{l,max}}}{h_\mathrm{l}^2\overline{v_0^*}} - \frac{4\mu_\mathrm{v}\overline{v}_{\mathrm{v,max}}}{h_\mathrm{l}R_\mathrm{v}\tau_{\mathrm{lv},0}^*}\right)\sqrt{\left(\frac{2\pi R_\mathrm{h}}{L_\mathrm{p}}\right)^2 + 1}. \tag{28}$$

The maximum liquid velocity in a groove is

$$\overline{v}_{\mathrm{l,max}} = \frac{\dot{Q}_\mathrm{g}}{\rho_\mathrm{l}A_\mathrm{l}h_\mathrm{fg}}. \tag{29}$$

Similarly, the maximum vapor velocity is

$$\overline{v}_{\mathrm{v,max}} = \frac{\dot{Q}_\mathrm{t}}{\pi R_\mathrm{v}^2\rho_\mathrm{v}h_\mathrm{fg}}, \tag{30}$$

where the total heat transported by the heat pipe accounts for the contributions by all of the individual grooves. Using the above relations, the liquid pressure drop in a groove as a function of the transported heat is

$$\Delta p_\mathrm{l} = \frac{L_\mathrm{eff}}{h_\mathrm{fg}}\left(\frac{\mu_\mathrm{l}\dot{Q}_\mathrm{g}}{h_\mathrm{l}^2\overline{v_0^*}\rho_\mathrm{l}A_\mathrm{l}} - \frac{4\mu_\mathrm{v}\dot{Q}_\mathrm{t}}{\pi h_\mathrm{l}R_\mathrm{v}^3\rho_\mathrm{v}\tau_{\mathrm{lv},0}^*}\right)\sqrt{\left(\frac{2\pi R_\mathrm{h}}{L_\mathrm{p}}\right)^2 + 1}. \tag{31}$$

The body forces imposed on the fluid within a particular groove may either aid or hinder the return of the fluid to the evaporator, depending on the groove pitch $L_\mathrm{p}$ and the circumferential location of the starting point of the helical groove [19,21]. However, even if the body force hinders the return of the fluid, each groove contributes to the heat transported $\dot{Q}_\mathrm{t}$. Therefore, the capillary limit equation (Eq. (23)) was first solved for the heat transported by each individual groove $\dot{Q}_\mathrm{g}$, and the results were summed to determine the total heat transport $\dot{Q}_\mathrm{t}$. Since the pressure drop in the vapor space and the pressure drop in each groove were functions of the total heat transport, Eq. (23) was solved iteratively. The body forces due to acceleration and gravity were integrated over the length of the groove to find the average pressure drop [19].

$$\Delta p_\mathrm{bf} = -\rho_\mathrm{l}\left[\int_0^{L_t}\hat{e}_{x_3}\cdot(-\vec{A} + \{-g\}\hat{e}_{z_1})\,\mathrm{d}s\right]\sqrt{\left(\frac{2\pi R_\mathrm{h}}{L_\mathrm{p}}\right)^2 + 1}. \tag{32}$$

Combining the above relations, the general expression for the maximum capillary limit for a single helical groove which accounts for shear stress at the liquid–vapor interface and the effect of groove fill ratio is given by

$$\begin{aligned}\frac{\sigma}{R_\mathrm{c}} \geqslant \frac{L_\mathrm{eff}}{h_\mathrm{fg}}&\left\{\frac{8\mu_\mathrm{v}\dot{Q}_\mathrm{t}}{\pi\rho_\mathrm{v}R_v^4} + \left(\frac{\mu_\mathrm{l}\dot{Q}_\mathrm{g}}{h_\mathrm{l}^2\overline{v_0^*}\rho_\mathrm{l}A_\mathrm{l}} - \frac{4\mu_\mathrm{v}\dot{Q}_\mathrm{t}}{\pi h_\mathrm{l}R_\mathrm{v}^3\rho_\mathrm{v}\tau_{\mathrm{lv},0}^*}\right)\right.\\ &\left.\times\sqrt{\left(\frac{2\pi R_\mathrm{h}}{L_\mathrm{p}}\right)^2 + 1}\right\}\\ &-\rho_\mathrm{l}\left[\int_0^{L_t}\hat{e}_{x_3}\cdot(-\vec{A} + \{-g\}\hat{e}_{z_1})\,\mathrm{d}s\right]\\ &\times\sqrt{\left(\frac{2\pi R_\mathrm{h}}{L_\mathrm{p}}\right)^2 + 1}.\end{aligned} \tag{33}$$

A closed-form solution for the capillary limit of a heat pipe with straight axial grooves and no body forces can be derived from Eq. (33).

$$\dot{Q}_\mathrm{cap} = \frac{\sigma h_\mathrm{fg}}{R_\mathrm{c}L_\mathrm{eff}}\left[\frac{\mu_\mathrm{l}}{N_\mathrm{g}h_\mathrm{l}^2\overline{v_0^*}\rho_\mathrm{l}A_\mathrm{l}} + \frac{8\mu_\mathrm{v}}{\pi\rho_\mathrm{v}R_\mathrm{v}^4}\left(1 - \frac{R_\mathrm{v}}{2h_\mathrm{l}\tau_{\mathrm{lv},0}^*}\right)\right]^{-1}. \tag{34}$$

Fig. 13(a) shows the results of the closed-form solution (Eq. (34)). The groove geometry given by Castle et al. [10] was used, except that straight axial grooves were assumed ($L_\mathrm{p} \to \infty$) instead of helical grooves. Over the range of groove fill ratio examined, the capillary limit increased with $A_\mathrm{l}/A_\mathrm{g}$ by more than three orders of magnitude. For this case, the semi-analytical solution and the two-point numerical solution were nearly identical due to the low vapor velocities, and hence the low liquid–vapor shear stress. This point is further demonstrated in Fig. 13(a) by the graph indicated by "No Shear", where the term in Eq. (34) that accounts for the effect of liquid–vapor shear on the liquid was dropped by allowing $\tau_{\mathrm{lv},0}^* \to -\infty$. The capillary limit decreases when shear stress is accounted for, as expected.

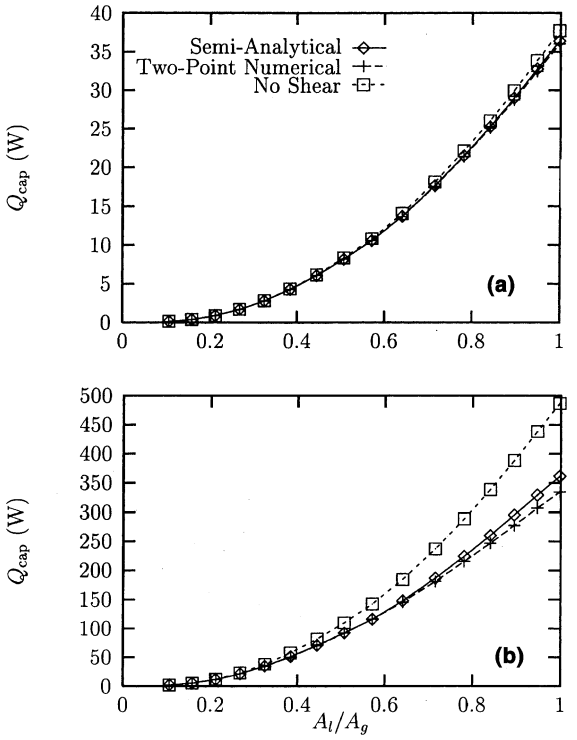


Fig. 13. Maximum heat transport predicted by the closed-form solution versus groove fill ratio (straight axial grooves, no body forces, $T_{sat} = 40°C$): (a) ethanol; (b) water.

Fig. 13(b) shows the closed-form solution when water is the working fluid. In this case, the difference between the results of the two-point numerical solution and the no-shear solution is much more pronounced due to the significantly higher vapor velocities involved. The agreement between the semi-analytical solution and the two-point numerical solution is quite good. The semi-analytical solution offers very close results with a significantly reduced amount of computer resources required.

The capillary limit prediction for the helically grooved heat pipe given by Eq. (33) is shown in Fig. 14 using the semi-analytical solution (Eq. (17)) for $|\vec{a}_r| = 0.0$ and 10.0-g. The capillary limit heat transport increases both with groove fill ratio and working temperature. In addition, $\dot{Q}_{cap}$ increases significantly with the radial acceleration due to the improved liquid pumping ability of the helical grooves [19].

The experimental data collected by Castle et al. [10] for the capillary limit of a revolving helically grooved heat pipe versus radial acceleration rates are shown in Fig. 15, along with the predictions of the present semi-analytical model and that given by Castle et al. [10]. During the experiments, the working temperature was not held constant, so the present model was evaluated at the saturation temperature reported for a given value of radial acceleration. For a groove fill ratio of $A_l/A_g = 0.5$ (Fig. 15(a)), the present model more closely matches the experimental data than the model by Castle et al. [10], which did not account for the groove fill ratio or liquid–vapor shear stress. For $A_l/A_g = 1.0$ (Fig. 15(b)), the present model significantly overpredicts the experimental data and the previous model, but matches the trend in the data quite well, given the simplicity of the model.

## 5. Conclusions

A numerical study has been concluded where the mean velocity, Poiseuille number, and volumetric flow rate of liquid in a trapezoidal groove have been determined as functions of groove geometry, meniscus contact angle and shear stress at the liquid–vapor interface. The mean velocity and volumetric flow rate have been shown to be linear functions of shear stress, and the Poiseuille number is a strong function of the shear stress

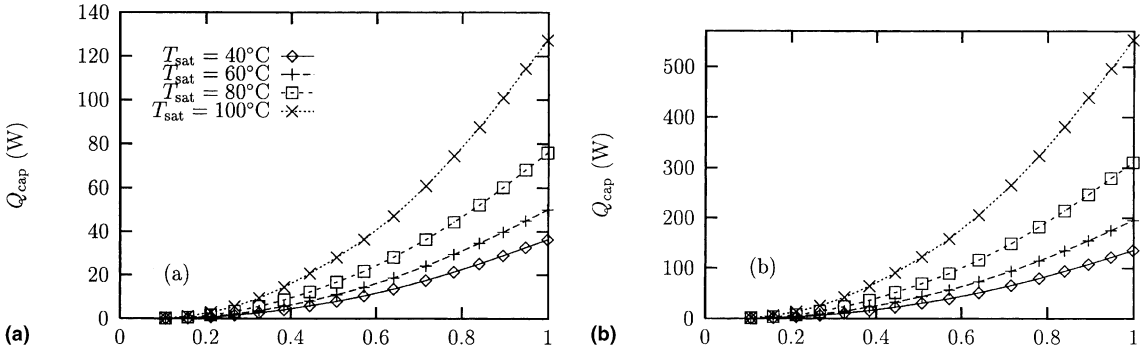


Fig. 14. Maximum heat transport versus groove fill ratio for several working temperatures (ethanol): (a) $|\vec{a}_r| = 0.0$-g; (b) $|\vec{a}_r| = 10.0$-g.

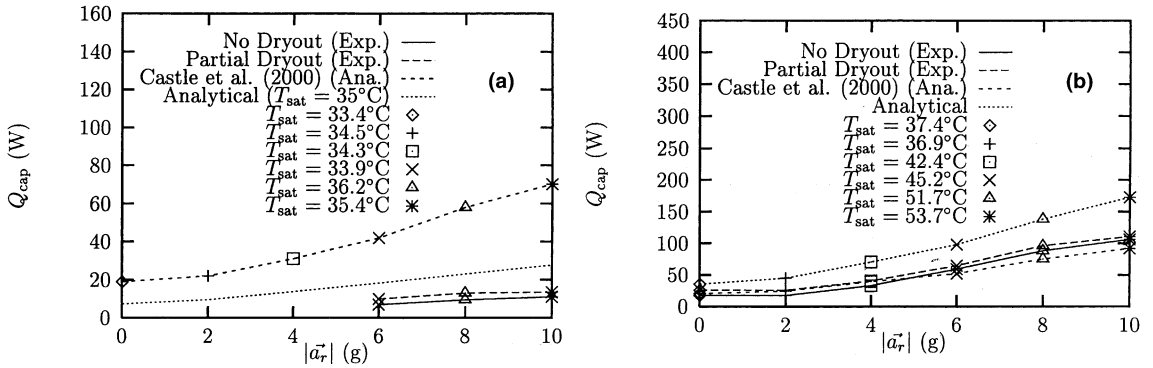


Fig. 15. Maximum heat transport versus radial acceleration: (a) $A_l/A_g = 0.5$; (b) $A_l/A_g = 1.0$.

for countercurrent flow. A semi-analytical solution and a two-point numerical solution for the mean velocity were presented and used to predict the capillary limit of a revolving helically grooved heat pipe for various groove fill ratios. Interfacial shear stress due to countercurrent flow in a heat pipe decreases the maximum heat transport. For cases in which the vapor velocities are high, this effect is more pronounced. The groove fill ratio was shown to have a significant impact on heat pipe performance. Underfilling the heat pipe examined by 10% resulted in a decrease in the predicted capillary limit by approximately 17–20% for water and ethanol, respectively.

## Acknowledgements

Funding for this work was provided by the Air Force Research Laboratory (PRPG) under Contract No. F33615-98-1-2844. Some of the computer resources were provided by the Ohio Supercomputer Center under Grant No. PNS394-2.

## References

[1] G. DiCola, Soluzionne analitica, amezzo della transformata di Fourier, di un problema di fusso in un canale rettangolare, Euratom CCR, Ispra, Italy, CETIS, 1968.
[2] G. Schneider, R. DeVos, Non-dimensional analysis for the heat transport capability of axially grooved heat pipes including liquid/vapor interaction, AIAA Paper No. 80-0214, 1980.
[3] P. Ayyaswamy, I. Catton, D. Edwards, Capillary flow in triangular grooves, ASME J. Appl. Mech. 41 (1974) 332–336.
[4] H. Ma, G. Peterson, X. Lu, The influence of vapor–liquid interactions on the liquid pressure drop in triangular microgrooves, Int. J. Heat Mass Transfer 37 (1994) 2211–2219.
[5] G. Peterson, H. Ma, Analysis of countercurrent liquid–vapor interactions and the effect on the liquid friction factor, Exp. Thermal Fluid Sci. 12 (1996) 13–24.
[6] L. Romero, F. Yost, Flow in an open channel, J. Fluid Mech. 322 (1996) 109–129.
[7] L. Lin, A. Faghri, Steady-state performance of a rotating miniature heat pipe, AIAA J. Thermophys. Heat Transfer 11 (1997) 513–518.
[8] D. Khrustalev, A. Faghri, Coupled liquid and vapor flow in miniature passages with micro grooves, ASME J. Heat Transfer 121 (1999) 729–733.
[9] J. Kolodziej, G. Musielak, M. Kaczmarek, T. Strek, Determination of free surface and gravitational flow of liquid in triangular groove, Comput. Mech. 24 (1999) 110–117.
[10] R. Castle, S. Thomas, K. Yerkes, The effect of working fluid inventory on the performance of revolving helically grooved heat pipes, in: Proceedings of the 2000 National Heat Transfer Conference, Paper No. NHTC2000-12268, Pittsburgh, PA, ASME J. Heat Transfer, 2000, in press.
[11] F. White, in: Viscous Fluid Flow, second ed., McGraw-Hill, New York, 1991.
[12] R. Burden, J. Faires, in: Numerical Analysis, third ed., PWS Publishers, Boston, 1985.
[13] R. Lykins, Numerical analysis of fully developed laminar flow in trapezoidal and sinusoidal grooves with shear stress at the liquid–vapor interface, Masters Thesis, Wright State University, Dayton, OH, 2000.
[14] R. Shah, Laminar flow friction and forced convection heat transfer in ducts of arbitrary geometry, Int. J. Heat Mass Transfer 18 (1975) 849–862.
[15] R. Shah, A. London, in: Laminar Flow Forced Convection in Ducts, Academic, New York, 1978.
[16] R. Hopkins, A. Faghri, D. Khrustalev, Flat miniature heat pipes with micro capillary grooves, ASME J. Heat Transfer 121 (1999) 102–109.
[17] E. Ruckenstein, R. Jain, Spontaneous rupture of thin liquid films, J. Chem. S. 70 (1974) 132–147.
[18] A. Faghri, in: Heat Pipe Science and Technology, Taylor and Francis, Washington, DC, 1995.
[19] S. Thomas, K. Klasing, K. Yerkes, The effects of transverse acceleration-induced body forces on the capillary limit of

helically grooved heat pipes, ASME J. Heat Transfer 120 (1998) 441–451.
[20] S. Chi, in: Heat Pipe Theory and Practice: A Sourcebook, Hemisphere, New York, 1976.
[21] K. Klasing, S. Thomas, K. Yerkes, Prediction of the operating limits of revolving helically grooved heat pipes, ASME J. Heat Transfer 121 (1999) 213–217.